Ebola virus infection induces a type I interferon response and the shutdown of key liver functions in human iPSC-derived hepatocytes

Whitney Manhart
National Emerging Infectious Disease Laboratory (NEIDL)
Liliana Mancio
Massachusetts Institute of Technology
Ellen Suder
National Emerging Infectious Disease Laboratory (NEIDL) https://orcid.org/0000-0001-9466-9204
Carlos Villacorta-Martin
Boston Medical Center
Jonathan Lindstrom-Vautrin
Center for Regenerative Medicine (CReM), Boston University and Boston Medical Center
John Bernbaum
Integrated Research Facility, National Institute for Allergy and Infectious Disease, National Institutes of Health
Steve Mazur
Integrated Research Facility, National Institute for Allergy and Infectious Disease, National Institutes of Health
Reed Johnson
National Institute of Allergy and Infectious Diseases
Aditya Mithal
Boston Medical Center https://orcid.org/0000-0002-8165-7674
Judith Olejnik
National Emerging Infectious Disease Laboratory (NEIDL)
Adam Hume
Boston University School of Medicine
Joseph Kaserman
Center for Regenerative Medicine of Boston University and Boston Medical Center
https://orcid.org/0000-0003-3334-5702
Andrew A Wilson
Boston University
Sangeeta Bhatia
Massachusetts Institute of Technology https://orcid.org/0000-0002-1293-2097

Elke Mühlberger
Boston University
Gustavo Mostoslavsky (gmostosl@bu.edu)
Boston Medical Center https://orcid.org/0000-0002-0784-2169

Article

Keywords: Ebola virus, liver function

Posted Date: March 26th, 2021

DOI: https://doi.org/10.21203/rs.3.rs-346554/v1

Abstract

Liver damage and an exacerbated inflammatory response are hallmarks of Ebola virus (EBOV) infection. Little is known about the intrinsic response to infection in human hepatocytes and their contribution to the observed inflammatory response. Here, we present an iPSC-derived hepatocyte platform to define the hepato-intrinsic response to EBOV infection. Transcriptomics analysis revealed a delayed host response with minimal transcriptomic changes at one day post infection (dpi) followed by a general downregulation of genes associated with hepatic functions and upregulation of interferon signaling at two and three dpi. Using RNA-FISH, we showed at single cell resolution that IFNβ and CXCL10 were mainly expressed in bystander cells or cells with weak EBOV mRNA signal intensity. We did not observe an inflammatory signature at any timepoint. In conclusion, iPSC-derived hepatocytes are an immune competent platform to study intrinsic responses to EBOV infection that have not been observed in EBOV-infected hepatocarcinoma cell lines.

Introduction

Ebola virus (EBOV) is a non-segmented negative sense (NNS) RNA virus and belongs to the family *Filoviridae* (1). EBOV infection causes a severe disease in humans with case fatality rates ranging from 40 to 90% (2). Despite the development of an approved EBOV vaccine and two promising antibody-based therapeutics (3, 4), there are currently no treatment options available to mitigate late stage Ebola virus disease (EVD).

Severe liver damage, coagulopathy, and thrombocytopenia are hallmark clinical manifestations of Ebola virus disease (EVD) (5). Histopathological changes in liver autopsies of fatal EBOV cases include hepatocellular necrosis, Councilman bodies, Kupffer cell hyperplasia, and the presence of EBOV inclusions in infected cells (5, 6). Circulating monocytes and macrophages have been identified as the earliest target cells in the liver of EBOV-infected nonhuman primates (NHPs) (7, 8). Infected Kupffer cells were detected as early as 3 days post infection (dpi) and infected hepatocytes by day 4 to 5 (8). Liver damage in EVD patients and experimentally infected NHPs is indicated by elevated serum levels of liver enzymes, including aspartate aminotransferase (AST), alanine aminotransferase (ALT), alkaline phosphatase, and γ-glutamyltransferase, and decreasing levels of albumin and calcium (8–12). Decreasing serum protein C levels and increasing fibrinogen levels indicate dysregulation of clotting and coagulopathy (13–15). In a low-dosage NHP EBOV infection, no significant changes in AST, ALT, or albumin levels were observed among the survivors, whereas the fatal cases exhibited changes in all of these markers, indicating severe liver damage (16). Massive hepatocyte apoptosis has been observed in murine models of EVD (17, 18), and two recent studies comparing EBOV and Reston virus pathogenesis in mice engrafted with human hematopoietic cells show that the magnitude of viral replication in the liver correlates with disease severity and fatal outcome (19, 20). Taken together, these reports indicate that the liver plays a pivotal role in severe EVD and therefore could be a target for therapeutic intervention.

In addition to organ damage, there is evidence that a dysregulated proinflammatory response is a hallmark of severe EVD (14). Monocytes and macrophages have been shown to be activated upon EBOV infection (7, 21–24), and this proinflammatory environment may impact liver damage during EBOV infection. While hepatocytes constitute over 80% of the liver volume, their immune response to EBOV has yet to be characterized. Most previous reports that have examined the intrinsic hepatic response to EBOV infection utilized immortalized hepatocarcinoma cell lines (25–28), which have an impaired antiviral response compared to primary human hepatocytes (PHHs) (29–32). While PHHs represent a more reliable platform, limited accessibility, donor-to-donor variability, and complex in vitro conditions required for long-term culture have restricted their use (33–36).

Here, we have employed human induced pluripotent stem cell (iPSC)-derived hepatocytes as a model for EBOV infection. These cells can be terminally differentiated and maintained in a monoculture for approximately 10 days and have previously been shown to effectively model viral infections (37–43). We demonstrate that iPSC-derived hepatocytes recapitulate aspects of the innate human host response to EBOV infection that cannot be modeled in immortalized cell lines. Our data show that EBOV infection leads to a delayed type I interferon (IFN) response and the downregulation of genes associated with liver function in iPSC-derived hepatocytes, illuminating a mechanism by which hepatocytes participate in EVD severity and liver damage.

Results

iPSC-derived hepatocytes are physiologically more similar to primary hepatocytes than immortalized Huh7 cells

To generate human hepatocyte-like cells from iPSCs, we used a previously published step-wise directed differentiation protocol that follows normal hepatic development as a roadmap for iPSC lineage specification (Fig. 1A) (39). At day 5 (D5), approximately 80–90% of the cells were CXCR4/cKit double-positive, indicating robust differentiation into definitive endoderm (Fig. 1B). By D20 of differentiation, most cells in culture adopted a cuboidal, highly vacuolated morphology, typical of primary hepatocytes (Fig. 1C). A molecular, histological and functional characterization of the iPSC-derived hepatocytes in comparison to either immortalized hepatocarcinoma Huh7 cells or fetal and adult liver tissue showed that the iPSC-derived hepatocytes retained expression of the fetal marker alpha feto protein (AFP), likely reflecting the embryonic-like characteristics of the cells in this culture system (Fig. 1D). As expected, iPSC-derived hepatocytes expressed many hepatic markers, including albumin, AAT and the transcription factors FOXA1, FOXA2 and HNF4a. The mRNA levels of these hepatic markers were generally higher in Huh7 cells compared to iPSC-derived hepatocytes. However, immunofluorescence analysis revealed striking differences in the protein levels and localization of the hepatic transcription factors in both cell types (Fig. 1E). While HNF4α, FOXA1, and FOXA2 were translocated into the nuclei of iPSC-derived hepatocytes, they were expressed at low protein levels in Huh7 cells and homogenously distributed throughout the cytoplasm. Albumin expression was observed in both cells types (Fig. 1E), whereas transferrin, a clotting factor and carrier protein produced exclusively by hepatocytes in the liver, was

robustly expressed in iPSC-derived hepatocytes but not in Huh7 cells (Fig. 1E), further emphasizing the differences between the two platforms. Functional analysis of iPSC-derived hepatocytes compared to Huh7 cells revealed major deficiencies in the Huh7 cells. One major function of hepatocytes *in vivo* is to store and metabolize lipoproteins, and an inability to bind or retain lipoproteins indicates a deficiency in hepatic function (44). While the majority of iPSC-derived hepatocytes were positive in the low-density lipoprotein (LDL) uptake assay, LDL uptake was impaired in Huh7 cells (Fig. 1F). Similarly, Periodic acid-Schiff (PAS) staining, used to detect glycogen storage, resulted in the typical magenta staining in the iPSC-derived hepatocytes, whereas the Huh7 cells showed weak and diffuse purple staining (Fig. 1G). Finally, we tested whether the iPSC-derived hepatocytes have a proper cytochrome P450 function. Hepatocytes produce cytochrome P450 enzymes, which are involved in the metabolism of over 80% of all prescribed therapeutics (45). Immortalized hepatocytes express low levels of these enzymes unless specifically cultured in confluent conditions (46). To measure the enzymatic activity of the predominant cytochrome P450 enzyme, CY3A4, in iPSC-derived hepatocytes and Huh7 cells, we used a luminescent-based assay. In contrast to Huh7 cells that had no CY3A4 activity, iPSC-derived hepatocytes showed a strong luminescent signal indicative of CY3A4 enzymatic activity (Fig. 1H).

It was previously reported that infection with vesicular stomatitis virus (VSV), a strong inducer of the type I IFN response, leads to type I IFN expression in PHHs but not in Huh7 cells (29). To examine if the iPSC-derived hepatocytes generated by us were able to adequately respond to an acute viral infection, iPSC-derived hepatocytes and Huh7 cells were infected with VSV and IFNβ expression was analyzed by qRT-PCR. In contrast to Huh7 cells, IFNβ expression was strongly upregulated in infected iPSC-derived hepatocytes (Fig. S1). This indicates that similar to PHHs, iPSC-derived hepatocytes are IFN-competent and able to respond to viral stimuli. It also confirms that hepatocarcinoma cell lines may not represent a suitable platform to analyze antiviral responses to viral infections.

Overall, these results indicate that iPSC-derived hepatocytes recapitulate functional and molecular hepatocyte features more faithfully than Huh7 cells do and therefore provide a better model to study EBOV hepatic infection.

iPSC-derived hepatocytes and primary human hepatocytes are susceptible to EBOV infection

Next, we determined if iPSC-derived hepatocytes were permissive to EBOV infection. As a comparison, we also infected primary human hepatocytes using a previously established platform based on cryopreserved adult primary hepatocytes collected from donors, allowing for the maintenance of primary hepatocytes in culture for up to several weeks (33, 34). We initially used micropatterned cocultures (MPCCs) that consist of PHH islands supported by J2-3T3 murine embryonic fibroblasts. The MPCC system was successfully used to for hepatitis C and hepatitis B virus infection studies (34). However, despite robust EBOV infection of the PHHs in this coculture system (Fig. S2A and B), the MPCCs were less suitable for EBOV because the mouse fibroblasts were infected as well in addition to the PHHs, albeit at low infection rates (Fig. S2A and B). Since the goal of this study was to dissect the host response of human hepatocytes to EBOV infection, infected mouse fibroblasts could potentially confound the results.

Therefore, we took advantage of a controlled apoptosis system to remove the 3T3-J2s fibroblasts from the MPCCs (47) prior to infection.

iPSC-derived hepatocytes from three different donors (BU1-3), PHHs from 2 donors in fibroblast-depleted MPCCs, and Huh7 cells were infected with EBOV over a time course of 7 days and analyzed by immunofluorescence staining. At 1 dpi, about 50% of iPSC-derived hepatocytes and PHHs were infected and about 90% of the Huh7 cells (Fig. 2A). Viral inclusion formation, a hallmark of EBOV infection, was observed in all three cell types (Fig. 2B). In parallel, we collected supernatants from the infected cells to determine viral titers over the course of infection. Viral titers peaked at 3 dpi, with the highest titers produced in Huh7 cells ($5x10^5$) followed by iPSC-derived hepatocytes ($2x10^4$) (Fig. 2C). The increase in viral titers correlated with an increase in the percentage of infected cells in culture, which consistently showed 80–90% infection by 3 dpi (Fig. 2A). Infected PHHs showed a modest increase in viral production and PHHs over time with overall lower titers ($1x10^3$) compared to the iPSC-derived hepatocytes. In summary, these data show that iPSC-derived hepatocytes and PHHs are permissive to EBOV infection and that iPSC-derived hepatocytes support EBOV replication more efficiently than PPHs do.

Since the iPSC-derived hepatocytes showed robust EBOV infection, we focused on this cell type for a more phenotypical characterization. To visualize spatial and temporal viral RNA production in infected cells at early and late time points, we performed single-cell, single-molecule RNA in situ hybridization using RNAscope technology (48). The used probes are directed against EBOV VP35 positive sense RNA which includes VP35 mRNA and antigenomic RNA. The positive sense antigenomic RNA is a complementary copy of the viral genome and serves as a replication intermediate (49). Robust viral mRNA production was observed at 8 hours post infection (hpi) with a punctate staining pattern throughout the cytoplasm, each small dot likely representing a single mRNA molecule, whereas larger bright puncta may represent RNA aggregates (48) (Fig. 3A). At 2 dpi, the viral RNA was homogenously distributed throughout the cytoplasm and aggregated in clusters that colocalize with viral inclusions (50).

Electron microscopy (EM) analysis of EBOV-infected iPSC-derived hepatocytes confirmed the formation of EBOV nucleocapsids in the cytoplasm of the infected cells and the release of viral particles (Fig. 3B). Newly synthesized EBOV nucleocapsids accumulated in viral inclusions and were arranged in parallel tubes in a hexagonal pattern in which each nucleocapsid is surrounded by 6 neighboring nucleocapsids, in line with previously reported observations (Fig. 3C) (51). The accumulation of viral inclusions and the release of viral particles was observed at 1 and 2 dpi for all 3 donors (Fig. 3D-F).

To follow the course of EBOV infection in iPSC-derived hepatocytes by live cell imaging, we used a recombinant EBOV clone expressing GFP from an additional transcription unit (52). Although the cells were infected with a high MOI of 10, we observed peak infection only at 3 dpi (Fig. S3). At 7 dpi, the infected cells showed a pronounced cytopathic effect (CPE), leading to reduced GFP expression. Overall, these data indicate that iPSC-derived hepatocytes can be productively infected with EBOV and that the infection leads to cell damage at late time points.

EBOV infection induces a delayed type I IFN response in human hepatocytes

To analyze the transcriptional profile induced by EBOV infection across the three infection platforms, iPSC-derived hepatocytes, PHHs, and Huh7 cells were infected with purified Ebola virions and the cellular RNA was harvested 24 hpi for bulk RNA sequencing analysis. The chosen time point was based on the transcriptional response to EBOV infection in human monocyte-derived macrophages, which display a strong transcriptional signature at 24 hpi (53). We calculated the log fold change (logFC) in expression for each aligned transcript between the EBOV-infected sample and mock control to determine which transcripts were differentially expressed for each condition. However, our results indicated that there was no significant differential gene expression in infected compared to noninfected cells in either cell type (Fig. S4).

It has been shown that delayed interferon responses to viral infections may contribute to disease severity (54, 55). In addition, we observed peak infection of EBOV-infected iPSC-derived hepatocytes as late as 3 dpi (Fig. S3). This inspired us to explore the transcriptional response to EBOV infection in liver cells at later time points. iPSC-derived hepatocytes were infected with EBOV and cellular RNA was isolated at 1, 2, 3, and 7 dpi for bulk transcriptomics analysis. Principle component analysis (PCA) of mock-infected compared to EBOV-infected samples at all time points showed clear clustering of the replicates, separating the non-infected from the infected samples at each time point, particularly at 2, 3 and 7 dpi (Fig. 4A). We observed minimal gene expression changes at 1 dpi, confirming our previous RNA sequencing data. When we ranked the expressed genes on normalized log counts per million (lcpm), there were only 14 upregulated genes and 18 downregulated genes with a p-value ≤ 0.01 at 1 dpi (Table S1). We then applied the same raw-normalized log counts per million (lcpm) analysis for the 250 most variable genes across all time points in mock-infected and EBOV-infected iPSC-derived hepatocytes over time and plotted the results as a heatmap (Fig. 4B). Clear gene expression signatures related to EBOV infection emerge at 2 and 3 dpi, converging into a different signature by 7 dpi. Starting 2 dpi, we observed a pronounced type I and III IFN signature, specifically upregulation of IFNβ, IFNλ1–3, and a set of IFN-stimulated genes (ISGs). There was a strong overlap of the top 30 DEGs at 2 and 3 dpi (20/30), including 13 ISGs (Fig. 4B, C and Fig. S5A). To further assess the induction of a type I/III IFN response in EBOV-infected cells, we plotted the fold change expression of a panel of type I/III IFNs, and 50 ISGs for each time point, confirming the upregulation of ISGs at 2 and even more pronounced, 3 dpi, including IFNλ1–3, IFNβ, chemokine ligand 5 (CCL5), 2'-5'-oligoadenylate synthetase like (OASL), OAS1, interferon-induced protein with tetratricopeptide repeats 1 (IFIT1), IFIT2, and the poorly characterized interferon-induced protein 44 (IFI44) that was shown to have antiviral activity (56–58) (Fig. 4C). By 7 dpi, the IFN response signature was no longer present (Fig. 4C).

A striking feature of the host response signature in the infected iPSC-derived hepatocytes was a general downregulation of genes at later time points, many of them associated with characteristic liver functions. For instance, several of the downregulated genes were associated with aminotransferases and ion transport (9/30) (Fig. S5B). AGXT, cytochrome P450 enzyme CYP3A7, the bile acid transporter nuclear receptor subfamily 1 group H member 4 (NRIH4), SERPINA7, ITIH1, and ITIH3 were all significantly

downregulated at 7 dpi (Fig. S5B). Genes involved in plasma formation and clotting, including ALB, insulin-like growth factor 2 (IGF2), podocan (PODN), and n-acetyltransferase 16 (NAT16), were also downregulated at this time point (4/30) (Fig. S5B). We further confirmed the significant downregulation of liver associated genes in EBOV-infected iPSC-derived hepatocytes 3 dpi by using a curated list of liver specific genes for comparison (39), including albumin (ALB), serpina genes (SERPINA 1 and SERPINA 3), fibrinogen genes (FGA, FGB, FGG), apolipoprotein genes (APOA1, APOA2 and APOC1) and angiopoetin (ANG) among others (Fig. 4D). This indicates that EBOV infection leads to severe liver cell damage associated with loss of hepatic functions.

To identify pathways which were perturbed during EBOV infection, we performed Gene Set Enrichment Analysis (GSEA) on the DEGs in EBOV-infected cells compared to mock-infected controls using WebGestalt (59). Gene ontology (GO) analysis showed moderate upregulation of IFN response pathways in EBOV-infected cells at 2 and 3 dpi (Fig. 5). Hallmark pathway analysis confirmed these results, highlighting that the IFNα and IFNγ response pathways are upregulated at 2 and 3 dpi (Table 1). Importantly, there was no upregulation of inflammatory response pathways, suggesting that EBOV infection does not trigger a proinflammatory response in primary-like hepatocytes. While there were only few moderately upregulated pathways in EBOV-infected cells, gene downregulation was more pronounced over the course of infection. This includes pathways related to metabolic processing, protein synthesis, protein transport, protein membrane localization, and extracellular structure organization, indicating cellular shutdown (Fig. 5). By Hallmark pathway analysis there were no upregulated pathways at 7 dpi (Table 1). By GO analysis, response to type I IFN and response to virus were slightly upregulated at 7 dpi, driven by the expression of IFNβ and IFNλ at this time point (Fig. 5). Hallmark pathway analysis suggested a downregulation of coagulation and xenobiotic metabolism pathways, indicating that EBOV-infected hepatocytes may have a reduced capacity to produce clotting factors or metabolize drugs, which are suggested implications of liver damage during EBOV infection of NHPs (Table 1) (8, 13).

Table 1

Summary of Hallmark Pathway Analysis of EBOV-infected iPSC-derived Hepatocytes. GSEA of Hallmark 50 Pathways for each time point of EBOV-infected iPSC-derived hepatocytes as compared to uninfected controls. Leading Edge Number represents the number of genes mapping to the hallmark pathway. Enrichment score is a measurement of the significance of the up or downregulation of the pathway based on the ranked genes that map to the particular pathway (closer to 1, more significantly upregulated; closer to -1, more significantly downregulated). Values greater than 0 are upregulated pathways, values less than 0 are downregulated pathways. FDR = false discovery rate. Parameters: minimum number of genes in a category = 15; FDR ≤ 0.01; number of permutations = 1000.

Time Point	Pathway	Leading Edge Number	Enrichment Score	FDR
1 dpi	N/A			
2 dpi	Interferon alpha response	29	0.69408	0
	Interferon gamma response	51	0.59635	0
	TNFA signaling via NFkB	60	0.45735	0.0053618
	Blood vessel formation	24	-0.70587	0
	Epithelial mesenchymal transition	97	-0.44221	0.00066813
	Biosynthesis of bile acids	35	-0.48976	0.00083516
	Metabolism of xenobiotics	69	-0.47167	0.00083516
	Blood coagulation cascade	51	-0.48574	0.0011135
3 dpi	Interferon alpha response	31	0.70268	0
	Interferon gamma response	46	0.58008	0
	Oxidative phosphorylation and citric acid cycle	116	-0.58008	0
	MYC targets, variant 1	80	-0.40318	0.0015312
	Blood vessel formation	16	-0.60886	0.0015312
	Adipocyte development	77	-0.37443	0.0020416
	Reactive oxygen species pathway	30	-0.51705	0.0020416
	Epithelial mesenchymal transition	78	-0.38571	0.0024499
	Blood coagulation cascade	45	-0.40118	0.0034998
7 dpi	Metabolism of xenobiotics	47	-0.48082	0
	Blood coagulation cascade	39	-0.62257	0
	Biosynthesis of bile acids	30	-0.48532	0.0012961
	Unfolded protein response; ER stress	33	-0.45886	0.0077766

Time Point	Pathway	Leading Edge Number	Enrichment Score	FDR
	Complement cascade	31	-0.41966	0.0089431
Average	Interferon alpha response	29	0.70338	0
	Interferon gamma response	49	0.58051	0
	Oxidative phosphorylation and citric acid cycle	114	-0.47009	0
	Blood vessel formation	18	-0.63409	0
	Blood coagulation cascade	56	-0.57744	0
	Epithelial mesenchymal transition	79	-0.42424	0.0005686
	Metabolism of xenobiotics	70	-0.41606	0.00090976
	Biosynthesis of bile acids	28	-0.44599	0.0015163
	MYC targets, variant 1	94	-0.38822	0.0055236
	Peroxisomes	37	-0.41766	0.0068232

We utilized WebGestalt to perform a transcription factor-based network analysis to determine the cis-elements that may be highly expressed and dominating the transcriptomic changes observed in our data. The major transcription factor targets based on the transcriptomic signature predicts that at 2 dpi the transcriptional response is directed by transcription factor binding to interferon-sensitive response element 1 (ISRE1) and an unknown gene set (Table S2). The unknown gene set is listed on the GSEA molecular signatures database (MSigDB) as 31 genes containing a highly conserved KRCTCNNNNMANAGC motif within 4 kb of the transcription start site. At 3 dpi, the network analysis predicts that the gene signature is dominated by transcription factor binding to ISRE1 and interferon regulatory factor 2 (IRF2), indicating an upregulation of the IFN response (Table S2). Finally, this network analysis of the DEGs at 7 dpi highlights that the gene expression profile is dominated by the activation of HNF1A, a hepatic-specific transcription factor that is critical for regulating cellular function in the adult liver (Table S2).

EBOV-infected iPSC-derived hepatocytes express IFNβ

Bulk RNA analysis only provides the average gene expression levels of a diverse cell population and does not allow to discriminate between the host response signatures in infected and non-infected cells. Given the clear but moderate type I/III IFN response in EBOV-infected iPSC-derived hepatocytes, we hypothesized that there might be significant heterogeneity regarding the IFN response in this cell population. To assess the IFN and inflammatory response at single cell level, we performed fluorescent in situ RNA hybridization (RNA-FISH) analysis with infected iPSC-derived hepatocytes using probes targeting IFNβ, CXCL10, and IL6 mRNA in combination with EBOV-specific probes targeting VP35 mRNA.

The number of the cells with detectable VP35 mRNA expression increased from about 20% at 1 dpi to 60–70% at 2 and 3 dpi (Fig. 6A and B). Consistent with the RNAseq data, less than 2% of the cells expressed CXCL10 (1.6%) or IFNβ (0.2%) at 1 dpi (Fig. 6A, C, and D). We observed an increase in both CXCL10 and IFNβ expressing cells at 2 and 3 dpi with up to 2% of IFNβ and 6% of CXCL10 expressing cells. Of note, CXCL10 and IFNβ were mainly expressed in uninfected bystander cells. The ratio of uninfected to infected IFNβ-expressing cells increased from 50% at day 1 to 92% at day 3 (Fig. S6A). Cells expressing IFNβ – particularly at 3 dpi – tended to be found in regions with a lower infection rate compared to the average infection rate of the whole slide. In addition, the signal intensity of EBOV mRNA was weak in cells expressing IFNβ or CXCL10, suggesting that these cells represent early stages of infection with low expression rates of VP35 and VP24, the known EBOV IFN antagonists (60). There was no detectable IL6 mRNA expression in infected iPSC-derived hepatocytes at any time point post infection, confirming the absence of an inflammatory response in these cells (Fig. S6B). In contrast to the iPSC-derived hepatocytes, we did not observe IFNβ or CXCL10 expression in Huh7 cells (Fig. S6C). Overall, the RNA-FISH results corroborate the findings from the transcriptomic analysis and suggest that EBOV infection of iPSC-derived hepatocytes induces a delayed and moderate type I IFN response that is not observed in infected Huh7 cells.

EBOV can be transmitted from infected macrophages to iPSC-derived hepatocytes. Since there is evidence that migrating monocytes or tissue-resident macrophages are early target cells in the liver (7, 8), we explored whether EBOV can be transmitted from infected macrophages to iPSC-derived hepatocytes in a co-culture model. Human primary monocyte-derived macrophages (MDMs) were infected with recombinant EBOV expressing GFP at a multiplicity of infection (MOI) of 10. One dpi, the cells were detached, rigorously washed, and seeded onto iPSC-derived hepatocytes. Spread of infection was visualized by GFP expression (Fig. 7). While only single green cells were observed at 2 dpi, likely representing infected MDMs, the infection spread throughout the entire iPSC-derived hepatocyte monolayer over the time course of 7 days, indicating that EBOV infection of hepatocytes can be initiated by infected macrophages.

Discussion

Although the liver plays a crucial role in EBOV disease, the intrinsic response of human hepatocytes to EBOV infection is not well defined. *In vitro* hepatocyte platforms are limited in their capacity to recapitulate human immune responses. Immortalized hepatocytes like Huh7 cells have impaired IRF3 signaling (29), which our study highlights as an important signaling cascade in the EBOV-induced hepatic host response. Additionally, investigations have shown that immortalized cell lines can vary significantly from lot to lot, preventing an accurate comparison of results across studies, even within the same cell line (61). PHHs are difficult to culture and require intricately engineered culture systems to support *in vitro* survival (33, 34). In the co-culture system presented in this study, PHHs destabilize 2 to 3 days after the removal of the fibroblast stroma (47) which challenges the use of this PHH culture system for longer infection times. For these reasons, we used iPSC-derived hepatocytes as an alternative to traditional immortalized and primary culture models. We have demonstrated that iPSC-derived hepatocytes are

terminally differentiated hepatocytes and primary-like in their functional capacity. iPSC-derived hepatocytes are also differentiated as a monoculture that can be sustained in a mature state for 10 days, allowing for longer infection studies than PHH culture systems. iPSC-based platforms also offer additional advantages, such as the ability to differentiate into multiple cell types from one donor to create organ-specific co-culture systems within one genetic background. This advantage is applicable to EBOV pathogenesis studies since EBOV infects many different cell types and organs, which may contribute to disease progression.

Using the iPSC-based platform, we began to define the intrinsic hepatic response to EBOV infection. The most prominent transcriptional changes are defined by downregulation of pathways involved in critical cellular processes, such as protein production and transport, and extracellular structure organization. This general shutdown of cell function is contrasted by a moderate upregulation of type I and type III IFN responses dominated by the expression of IFNβ, IFNλ1, and select ISGs beginning 2 dpi and increasing at 3 dpi. At single cell level, IFNβ and CXCL10 expression was observed in uninfected cells and cells with low expression levels of EBOV mRNA. This is in line with RNA-FISH analysis on liver samples obtained from EBOV-infected NHPs, showing expression in uninfected bystander cells (7). Although EBOV generally suppresses type I IFN induction in the infected cells (62), there is a strong proinflammatory and IFN response in EVD patients and infected animals associated with specialized immune cells, including macrophages and monocytes (7, 14, 24, 53, 63, 64). In contrast to monocytes and macrophages, there was no induction of a proinflammatory response in EBOV-infected iPSC-derived human hepatocytes, indicating that, indeed, immune cells are the main drivers of EBOV-induced inflammation (23, 24).

A crucial question that still needs to be addressed from our observations is that hepatocytes are consistently silent 1 dpi, despite significant infection at this time point. This delayed antiviral response might provide an environment that favors undisturbed viral propagation. Along the same lines, although the iPSC-derived hepatocytes are IFN-competent, the IFN response to EBOV infection still remains moderate at later time points and seems incapable of controlling viral spread. We do not yet understand if this attenuated response in both infected and uninfected cells can solely be attributed to EBOV's ability to antagonize innate immune responses or if there are additional mechanisms in place that interfere with cell-to-cell communication. This lag in antiviral response may open a window for early therapeutic intervention through stimulating an antiviral response by inducing IFN production in uninfected bystander cells. Indeed, FDA approved therapeutics that stimulate antiviral responses have been shown to inhibit EBOV infection in immortalized cell culture systems (65).

Another critical component of the hepatic response to EBOV infection is the downregulation of coagulation and acute phase reactant pathways beginning 2 dpi. Coagulopathy is a well-established clinical indicator of severe EBOV infection, although the exact impact of consumptive coagulopathy or disseminated intravascular coagulation (DIC) on the pathogenesis of EVD is poorly understood (66). Increasing levels of fibrin in whole blood samples is associated with fatality in EBOV patients, and in a study of 5 patients, fibrinogen D-dimer products in whole blood decreased in patients who survived infection (14, 15). Tissue factor (F3) is also upregulated in EBOV infection, and inhibition of F3 was

protective against EBOV infection in NHPs (5, 6, 8, 13, 67, 68). In our study, iPSC-derived hepatocytes downregulate the coagulation cascade 2–7 dpi. We also do not observe an increase in acute phase reactants that has been observed in NHPs (69). iPSC-derived hepatocytes downregulate the expression of critical clotting factors and plasma proteins, including ALB, fibrinogen chains alpha, beta, and gamma (FGA, FGB, and FGG), protein c (PROC), and F3 as early as 2 dpi. This discrepancy could be evidence of a compensatory feedback loop designed to prevent coagulation dysfunction or consumptive coagulopathy. Fibrinogen levels are lower than healthy controls in EBOV patients and increase in patients who survive, and low levels of serum ALB is a hallmark indicator of EBOV-induced liver damage in NHPs (15, 70). This is emphasized by the network analysis of the 7 dpi DEG that highlighted HNF1A as a critical regulator of the gene expression profile. In EBOV-infected NHPs, another hepatic nuclear factor homeobox gene (HNF4A) was significantly downregulated in the liver, and the authors attributed the downregulation of this transcription factor with the associated downregulation of genes involved in cholesterol synthesis, coagulation, and hepatic metabolism (71). HNF1A is known to regulate the expression of HNF4A and can bind to its promoter, which may highlight overlap in the transcriptional signatures between our EBOV-infected iPSC-derived hepatocytes and bulk NHP liver tissue (71, 72). Of the HNF4A targets listed in this study as downregulated transcripts in the liver, we observe significant downregulation in 11/17 genes (PCK2, PDK4, APOB, CYP3A7, CYP2A6, F7, TF, F3, TTR, and SERPINC1) (71). Clearly, the expression of coagulation factors in hepatocytes is impacted during EBOV infection, but the role that this may play in pathogenesis, organ failure, or patient outcome is poorly understood. This platform allows for further investigation of the hepatic responses to EBOV infection that can help elucidate the complex mechanisms which underlie liver pathology infection and help identify targets for therapeutic interventions that may universally prevent EBOV fatality.

Materials And Methods Short

iPSC Culture and Directed Differentiation into Hepatocytes

iPSCs were maintained on matrigel-coated 6-well tissue culture plates in 2 mL of mTeSR 1 feeder-free medium (STEMCELL Technologies) with 200 ng/mL Primocin (Invitrogen) and incubated at 37°C/5% CO_2. The directed differentiation from iPSCs into hepatocytes was performed as previously described (39). After D0, the cells were incubated in hypoxic conditions at 37°C. For D1-D5 of the differentiation protocol, the STEMdiff Definitive Endoderm kit (STEMCELL Technologies) was used according to manufacturer's instructions.

Immortalized Cell Culture

Vero E6 (Cercopithecus aethiops kidney cell line, ATCC CRL-1586) and Huh-7 cells (human hepatocellular carcinoma cell line, provided by J. Alonso, Texas Biomedical Research Institute, San Antonio, TX) were maintained in Dulbecco's Modified Eagle Media (DMEM) (Gibco), 10% fetal bovine serum (FBS), 200 nM L-glutamine in solution, and 5000 units/mL Penicillin Streptomycin solution. Cells were incubated at 37°C with 5% CO_2.

Primary Hepatocyte Cell Culture

The PHH co-culture with murine embryonic fibroblasts 3T3-J2s were generated by seeding cryopreserved primary human hepatocytes purchased from BioIVT on collagen-patterned 96-well plates as described previously (33, 34). 3T3-J2s were a kind gift provided by Howard Green (Harvard Medical School). Fibroblast-depleted micropatterned PHH cultures were obtained by incorporation of 3T3-J2s expressing an inducible apoptosis switch (inducible caspase-9, Casp9). 3T3-J2s were lentivirally transduced with the pMSCV-F-del Casp9.IRES.GFP plasmid (15567, Addgene) followed by FACS purification (top 15%, FACSAria II, BD Biosciences) (47). On the day of infection, PHH co-cultures were dosed with a chemical inducer of dimerization (0.5 μM AP20187, Takarabio) to trigger fibroblast removal via apoptosis. PHH co-cultures were maintained in Dulbecco's Modified Eagle Medium (DMEM, Corning) supplemented with 10% fetal bovine serum (Gibco), 1% ITS (insulin/transferrin/selenous acid and linoleic acid, BD Biosciences), 7 ng/mL glucagon (Sigma-Aldrich), 40 ng/mL dexamethasone (Sigma-Aldrich), 15 mM HEPES (Gibco), and 100 μg/mL penicillin-streptomycin (Corning). Cells were kept at 37C with 5% CO2.

Virus Infection And Purification

Work with infectious EBOV was performed at Boston University's National Emerging Infectious Diseases Laboratories, Boston, MA and at the NIH/NIAID Integrated Research Facility, Fort Detrick, MD. EBOV isolate Mayinga (GenBank accession number AF086833.2; kindly provided by H. Feldmann, NIH NIAID Rocky Mountain Laboratories, Hamilton, MT) and recombinant EBOV-GFP (Mayinga isolate; kindly provided by the World Reference Center for Emerging Viruses and Arboviruses, University of Texas Medical Branch, Galveston, TX) expressing green fluorescence protein (GFP) from an additional transcription unit (52) were propagated in Vero E6 cells as described before (53). Cell supernatants were centrifuged at 1,000xg for 10 minutes at 4°C to remove cellular debris. To remove soluble factors, including cytokines and chemokines, clarified supernatants were purified over a 20% sucrose cushion by centrifugation at 25,000 rpm for 2 hours at 4°C and the pelleted viral particles were resuspended on PBS. Viral titers were determined by tissue culture infectious dose 50 ($TCID_{50}$) assays and focus forming unit (FFU) assays as previously described (53). Recombinant vesicular stomatitis virus (VSV) expressing GFP or mCherry from an additional transcription unit (VSV-GFP and VSV-mCherry; kindly provided by J. Connor, Boston University) was propagated in Vero E6. Viral titers were determined by $TCID_{50}$.

All EBOV infection studies were performed with purified virions. If not stated otherwise, cells were infected at a multiplicity of infection (MOI) of 10 for infection studies. After addition of the inoculum, virions were allowed to adsorb for 20 minutes to 1 hour at 37ºC before cells were washed and fresh cell culture medium was added.

Flow Cytometry Analysis

$2.5x10^5$ cells D0 and D5 cells were stained for flow cytometry analysis of the endoderm markers cKit and CXCR4. Cells were harvested by centrifugation at 300xg at 4°C for 5 minutes. Cells were resuspended in PBS and stained with APC-conjugated cKit (BioLegend) and PE-conjugated CXCR4 (Invitrogen) primary

antibodies for 30 minutes. Cells were washed with FACS buffer and filtered through a 35 µm filter into a 5 mL polystyrene FACS tube and analyzed on a Stratadigm Flow Cytometry machine or a FACS Calibur Flow Cytometry machine. Analysis of the flow plots was performed using FlowJo.

qRT-PCR Analysis

Cells were harvested for RNA analysis by using either the RNeasy Kit (Qiagen) or TRIzol Reagent (ThermoFisher) according to manufacturer's instructions. For hepatic cellular markers, the TaqMan qRT-PCR system (ThermoFisher) was used. cDNA libraries of the harvested cellular RNA were prepared using SuperScript III Reverse Transcriptase (ThermoFisher). 500 ng of the cDNA library was added to a TaqMan probe reaction master mix containing 10 µL of the TaqMan Universal PCR Master Mix 2x Buffer, 1 µL of TaqMan gene probe, and nuclease-free water to a final volume of 20 µL per reaction. For qRT-PCR of IFNβ, $1x10^6$ or $4x10^5$ iPSC-derived hepatocytes and Huh7 cells were harvested 1 day post-VSV infection by using TRIzol Reagent (ThermoFisher) according to manufacturer's instructions. The QuantiTect SYBR Green RT-PCR kit was used (Qiagen) for qRT-PCR analysis. 50 ng of purified cellular RNA was added to a SYBR Green reaction master mix containing 12.5 µL of SYBR master mix, 2.5 µL of QuantiTect gene probe, 0.25 µL of QuantiTect Reverse Transcriptase mix, and nuclease-free water to a final volume of 25 µL per reaction. For both systems, samples were run on a StepOnePlus Real Time PCR machine (ThermoFisher). CT values were plotted using Prism GraphPad Software. Statistical significance was determined by paired t-tests with comparisons of interest plotted on each graph.

Periodic Acid-Schiff (PAS) Staining

PAS staining was performed on $1x10^6$ iPSC-derived hepatocytes or Huh7 cells using the Periodic Acid-Schiff (PAS) kit (Sigma-Aldrich) according to manufacturer's instructions. Cells were fixed with 1 mL of 4% paraformaldehyde (PFA) solution for 10 minutes at room temperature prior to PAS staining. PBS was added to the cells for imaging on an inverted microscope.

LDL-Uptake Assay

$1x10^6$ D0 cells, iPSC-derived hepatocytes, and Huh7 cells were analyzed using the LDL Uptake Assay Kit (Cell-Based) (Abcam) according to manufacturer's instructions. The LDL-DyLight reagent was diluted in the appropriate cell culture medium for each cell type. The cells were incubated with the LDL reagents at 37°C for 4 hours. Cells were washed one time with 1 mL of PBS, and 2 mL of PBS was added to the cells for visualization of LDL update on an inverted microscope with a filter capable of capturing excitation and emission wavelengths of 540 and 570 nm.

CYP3A4 P450-Glo Assay

The quantification of CYP3A4 in $1x10^6$ iPSCs, iPSC-derived hepatocytes, and Huh7 cells was performed using the P450-Glo Assay kit (Promega) according to manufacturer's instructions. One day prior to the assay, Huh7 cells were treated with cell culture media containing 100 nM Dexamethasone. One the day of

the assay, the Luciferin Glo substrate was added to the appropriate cell culture medium for each cell type. Cells were incubated with luciferin reagents at 37°C for 4 hours. Supernatant was clarified at 300xg for 5 minutes at room temperature. Clarified supernatant and detection reagent were incubated at room temperature for 20 minutes. Luminescence was measured on a LUMIStar Omega Luminometer (BMG Labtech).

Immunofluorescence Analysis

$1x10^6$ or $4x10^5$ cells were fixed with either 4% PFA in DMEM for 10 minutes at room temperature or 10% formalin for at least 6 hours at 4°C. Cells were washed in PBS, permeabilized with a solution of acetone-methanol in a 1:1 volume ratio for 5 minutes at -20°C, and incubated in blocking buffer for at least 20 minutes at room temperature. Due to cross-reactivity with the BSA in the blocking buffer, the cells were not incubated in blocking buffer when stained for albumin. Cells were incubated with primary antibody overnight at 4°C, and primary antibody names and dilutions are listed in Table 2. Cells were incubated with secondary antibody and 4',6-diamidino-2-phenylindole (DAPI) for one hour at room temperature (dilutions listed in Table 2).

Table 2
Antibodies used for immunofluorescence analysis.

Antigen	Company	Species	Dilution
Albumin	Dako	Rabbit	1:100
Alexa Fluor α-mouse 594	Thermo Fisher	Donkey	1:200
Alexa Fluor α- rabbit 488	Thermo Fisher	Goat	1:200
Alexa Fluor α-goat 488	Thermo Fisher	Donkey	1:200
CK18, human	Abcam	Rabbit	1:100
EBOV NP	Gift from G. Olinger, USAMRIID	Mouse	1:200
EBOV VP35	Antagene, custom	Goat	1:1000
EBOV VP40	BEI	Mouse	1:200
FOXA1	Abcam	Rabbit	1:100
FOXA2	Abcam	Rabbit	1:100
HNF4α	Abcam	Mouse	1:50
NFκB p65 (A)	Santa Cruz	Rabbit	1:200
Transferrin	ThermoFisher	Rabbit	1:50

VSV Bioassay

$4x10^5$ iPSC-derived hepatocytes from 3 donors and triplicate samples of Huh7 cells were infected with VSV-GFP or VSV-mCherry at an MOI of 10. 1 dpi, cells were imaged for GFP expression and cellular RNA was purified for qRT-PCR analysis.

LPS stimulation for NFκB Activation

$4x10^5$ iPSC-derived hepatocytes from three donors were treated with 300 ng of Ultrapure LPS (Invitrogen) diluted in D19 medium for 1 hour at 37°C and 5%CO_2. Cells were fixed and used for immunofluorescence analysis.

Electron Microscopy

For conventional thin-section microscopic evaluation, $4x10^5$ EBOV-infected iPSC-derived hepatocytes were inactivated and preserved in 2.5% glutaraldehyde (E.M. Sciences, Warrington, PA), in Millonig's sodium phosphate buffer (Tousimis Research, Rockville, MD), for 24 hours. After fixation was complete, the cells were washed in Millonig's buffer, and incubated for two hours in 1.0% osmium tetroxide, in the same buffer. Following rinsing steps in ultrapure water and en bloc staining with 2.0% uranyl acetate, the samples were dehydrated in a series of graded ethanol washes and infiltrated and embedded in Spurr's plastic resin (E.M. Sciences). Embedded blocks were sectioned using a Leica UC7 Ultramicrotome. 70–80 nm sections were collected on 200 mesh copper grids, and post-stained with Reynold's lead citrate. Samples were examined in a FEI Tecnai Spirit Twin transmission electron microscope, operating at 80 kV.

SmartSeq2 Sequencing

$1x10^6$ iPSC-derived hepatocytes or Huh7 cells were seeded in 6-well tissue culture plates, and $1x10^4$ PHHs were seeded in 96-well glass-bottom plates. The cells were infected with EBOV at an MOI of 10 or left uninfected and lysed 1 dpi. Cellular RNA was isolated using TRIzol reagent (ThermoFisher) according to the manufacturer's instructions. 50 ng of purified RNA was used for sequencing by diluting to a final concentration of 5 ng/µL in a final volume of 10 µL. Samples were pipetted into a twin.tec® PCR 96-well plate (Eppendorf) and sent out for sequencing on dry ice. Sequencing was performed at the Broad Institute Genomics Services Core. The quality of the raw data was assessed using FastQC v.0.11.7. The sequence reads were aligned to a combination of the human genome reference (GRCh38) and the Ebola virus reference (NC_002549.1) using STAR v.2.6.0c. Counts per gene were summarized using the featureCounts function from the subread package v.1.6.2. The matrix of counts per gene per sample was then analyzed using the limma/voom normalization (limma v. 3.39.19, edgeR v.3.25.10). After exploratory data analysis (Glimma v. 1.11.1), contrasts for differential expression testing were done for each EBOV-infected sample compared to mock-infected samples (controls) at each time point separately. Functional predictions were performed using WebGestalt for gene set analysis (59).

Illumina Sequencing

$1x10^6$ iPSC-derived hepatocytes were mock-infected or infected with EBOV at an MOI of 10. Cells were harvested for RNA analysis at 1, 2, 3, and 7 dpi using TRIzol reagent (ThermoFisher). RNA was isolated according to manufacturer's instructions. 1 µg of purified cellular RNA was diluted to a concentration of 50 ng/µL in a final volume of 20 µL and shipped to Novogene on dry ice for library preparation and Illumina sequencing. The quality of the raw data was assessed using FastQC v.0.11.7. The sequence reads were aligned to a combination of the human genome reference (GRCh38) and the EBOV reference sequence (NC_002549.1) using STAR v.2.6.0c. Counts per gene were summarized using the featureCounts function from the subread package v.1.6.2. The matrix of counts per gene per sample was then analyzed using the limma/voom normalization (limma v. 3.39.19, edgeR v.3.25.10). After exploratory data analysis (Glimma v. 1.11.1), contrasts for differential expression testing were done for each EBOV-infected sample compared to the mock control at each time point separately. Statistical significance of the logFC for each time point contrast was determined by a paired t-test and reported as a Benjamini-Hochberg false discovery rate adjusted p-value. Gene Set Enrichment Analysis (GSEA) was performed using all genes in the dataset, ranked on logFC, using WebGestalt to analyze Biological Processes in GO databases or the Reactome in Pathway databases with the following parameters: minimum number of genes in a category = 15; false discovery rate (FDR) $\leq$ 0.01; permutations = 1000 (59).

Fluorescent In-situ Hybridization Assay

Fluroescent in-situ hybridization (RNA-FISH) was performed using the Advanced Cell Diagnostics RNAscope v2 kit according to manufacturer's instructions (ACD Bio). $5x10^5$ iPSC-derived hepatocytes were seeded onto 2 well glass chamber slides, and $1x10^5$ Huh7 cells were seeded onto 8 well glass chamber slides. Both cell types were infected at an MOI of 10 as described above. Cells were fixed with 10% formalin for a minimum of 6 hours. After fixation, cells were dehydrated with ethanol washes before being stored in 100% ethanol at -20ºC until staining. On the day of the assay, cells were rehydrated with ethanol. Cells were pre-treated with hydrogen peroxidase and Protease III according to the manufacturer's instructions. Cells were probed with RNAscope probes for 2 hours at 40ºC in the ACD hybridization oven. The following probes (all from ACD Bio) were used: ebolavirus Zaire VP35- C1 (undiluted), human IL6- C2 (1:50), human IFNβ- C3 (1:50), human CXCL10- C3 (1:50). After hybridization, the cells were treated with the amplification and development reagents according to manufacturer's instructions. An additional blocking and washing step was added following amplification of channels containing viral RNA probes to prevent cross-reaction due to viral gene abundance. Fluorophores used for detection (Perkin Elmer) include Opal 520 (1:3000), Opal 570 (1:3000), and Opal 690 (1:1500). Samples were visualized on a Nikon Eclipse Ti2 inverted microscope using Photometrics Prime BSI camera, and quantification of gene-expressing cells was performed in QuPath (cite) software (https://doi.org/10.1038/s41598-017-17204-50) using the cell detection feature and manual identification of positive cells.

Macrophage Differentiation From Peripheral Mononuclear Blood Cells

MDMs were generated from leukopaks (NY Biologics Inc.) or apheresed peripheral blood mononuclear cells (PBMCs) using Ficoll separation (GE Healthcare). Whole blood was diluted to a final volume of 30 mL with PBS. 15 mL of Ficoll was added to a 50 mL conical tube, and the diluted whole blood was overlayed onto the Ficoll. Blood was centrifuged for 30 minutes at 450xg with the brake turned off of the centrifuge. The blood separated into three layers: the off-white plasma layer, a thin white buffy coat containing leukocytes, and the pelleted erythrocytes. The plasma layer was removed, and the buffy coat was isolated into a fresh 50 mL conical tube. The buffy coat was diluted to a final volume of 50 mL using 37ºC PBS. Cells were centrifuged at 350xg for 10 minutes with the centrifuge brake on. The cell pellet was then washed three times with 50 mL of warm PBS and centrifuged at 350xg for 10 minutes. After the final wash, cells were resuspended in 1 mL of warm PBS and counted. $1x10^7$ cells were plated in a T75 flask with RPMI medium for one hour at 37ºC and 5% CO_2, non-adhered cells were removed, and 10 ml RPMI medium with 10% FBS, 1% L-glutamine, 10 mM HEPES, 10ng/mL GM-CSF, and 50 U/mL penicillin with 50 mg/mL streptomycin (MDM medium) was added to the cells. Medium was changed every 2 to 3 days for a minimum of 6 days before differentiated macrophages were split into 6-well TC plates for infection experiments.

Co-Culture of iPSC-Derived Hepatocytes and Macrophages

On the day prior to infection, MDMs seeded in a T75 flask were split by incubating cells with 0.1% Trypsin-EDTA solution for 15 minutes at 37°C and 5%CO_2. Cells were centrifuged at 300xg for 5 minutes at 4°C and resuspended in 1 mL of MDM medium. Cells were counted and $1x10^6$ cells were seeded into 6-well low-attachment plates (Corning). On the day of infection, macrophages were infected with EBOV-GFP at an MOI of 10. At 1 dpi, MDMs were incubated with 1 mL of Gentle Cell Dissociation buffer (GCD; Gibco) for 2 minutes at 37°C and 5%CO_2. Cells were centrifuged at 300xg for 5 minutes at 4°C. GCD was removed, and cell pellets were washed three times in 1 mL of PBS. After the third wash, cells were resuspended in 1 mL of the appropriate medium and seeded in 6- or 12-well tissue culture plates alone or onto D20 iPSC-derived hepatocytes at a 1:1 ratio.

Declarations

Acknowledgments

We would like to thank Jennifer Pacheco for excellent technical support, H. Feldmann, Rocky Mountain Laboratories and the World Reference Center for Emerging Viruses and Arboviruses for providing virus stocks, and G. Olinger and the Defense Biological Product Assurance Office (DBPAO) through BEI for providing antibodies.

Funding: This work was supported by NIH NIAID grants R21AI137793 (to G.M. and E.M.), R21AI135912 (to E.M.), and R01 AI133486 (to E.M.). S.N.B. is a Howard Hughes Medical Institute Investigator.

Author Contributions: W.A.M. differentiated iPSC-derived hepatocytes, performed EBOV infection studies and most of the post-infection experiments, was involved in data analysis, and wrote the first draft of the manuscript. L.M.S. generated primary hepatocyte cultures. C.V.M. and J.V.L performed bioinformatics analyses. J.G.B. performed the electron microscopy analysis. S.M., R.F.J., and A.J.H. performed BSL-4 infection studies. E.L.S. performed FISH analysis, imaging, and image quantification. A.M. and J.O. performed RNA analysis. S.N.B. was involved in the design of the primary hepatocyte experiments. E.M. and G.M. designed and directed the study, performed data analysis and interpretation, and edited the manuscript.

Competing Interests: The authors declare no competing interests.

Data and materials availability: All data needed to evaluate the conclusions in the paper are present in the paper and/or the Supplementary Materials. Submission of the RNA sequencing data to Gene Expression Omnibus (GEO) is pending. Pluripotent stem cell lines used in this study, along with maintenance standard operating procedures and directed differentiation protocols are available from the CReM iPSC Repository at Boston University and Boston Medical Center and can be found at http://www.bu.edu/dbin/stemcells/.

References

1. J. H. Kuhn *et al.*, ICTV Virus Taxonomy Profile: Filoviridae. *J Gen Virol* **in press**, (2019).
2. C. Munoz-Fontela, A. K. McElroy, Ebola Virus Disease in Humans: Pathophysiology and Immunity. *Curr Top Microbiol Immunol* **411**, 141-169 (2017).
3. S. Mulangu *et al.*, A Randomized, Controlled Trial of Ebola Virus Disease Therapeutics. *N Engl J Med* **381**, 2293-2303 (2019).
4. E. Callaway, 'Make Ebola a thing of the past': first vaccine against deadly virus approved. *Nature* **575**, 425-426 (2019).
5. R. B. Martines, D. L. Ng, P. W. Greer, P. E. Rollin, S. R. Zaki, Tissue and cellular tropism, pathology and pathogenesis of Ebola and Marburg viruses. *J Pathol* **235**, 153-174 (2015).
6. S. R. Zaki, C. S. Goldsmith, Pathologic features of filovirus infections in humans. *Curr Top Microbiol Immunol* **235**, 97-116 (1999).
7. A. R. Greenberg *et al.*, Quantification of Viral and Host Biomarkers in the Liver of Rhesus Macaques: A Longitudinal Study of Zaire Ebolavirus Strain Kikwit (EBOV/Kik). *Am J Pathol*, (2020).
8. T. W. Geisbert *et al.*, Pathogenesis of Ebola hemorrhagic fever in cynomolgus macaques: evidence that dendritic cells are early and sustained targets of infection. *Am J Pathol* **163**, 2347-2370 (2003).
9. S. Lanini *et al.*, Relationship Between Viremia and Specific Organ Damage in Ebola Patients: A Cohort Study. *Clin Infect Dis* **66**, 36-44 (2018).
10. E. de Wit *et al.*, Clinical Chemistry of Patients With Ebola in Monrovia, Liberia. *J Infect Dis* **214**, S303-S307 (2016).

11. T. M. Uyeki *et al.*, Clinical Management of Ebola Virus Disease in the United States and Europe. *N Engl J Med* **374**, 636-646 (2016).
12. P. E. Rollin, D. G. Bausch, A. Sanchez, Blood chemistry measurements and D-Dimer levels associated with fatal and nonfatal outcomes in humans infected with Sudan Ebola virus. *J Infect Dis* **196 Suppl 2**, S364-371 (2007).
13. T. W. Geisbert *et al.*, Mechanisms underlying coagulation abnormalities in ebola hemorrhagic fever: overexpression of tissue factor in primate monocytes/macrophages is a key event. *J Infect Dis* **188**, 1618-1629 (2003).
14. X. Liu *et al.*, Transcriptomic signatures differentiate survival from fatal outcomes in humans infected with Ebola virus. *Genome Biol* **18**, 4 (2017).
15. S. J. Smither *et al.*, Haemostatic Changes in Five Patients Infected with Ebola Virus. *Viruses* **11**, (2019).
16. K. J. Alfson *et al.*, Intramuscular Exposure of Macaca fascicularis to Low Doses of Low Passage- or Cell Culture-Adapted Sudan Virus or Ebola Virus. *Viruses* **10**, (2018).
17. S. B. Bradfute *et al.*, Mechanisms and consequences of ebolavirus-induced lymphocyte apoptosis. *J Immunol* **184**, 327-335 (2010).
18. A. L. Rasmussen *et al.*, Host genetic diversity enables Ebola hemorrhagic fever pathogenesis and resistance. *Science* **346**, 987-991 (2014).
19. J. R. Spengler *et al.*, Severity of Disease in Humanized Mice Infected With Ebola Virus or Reston Virus Is Associated With Magnitude of Early Viral Replication in Liver. *J Infect Dis* **217**, 58-63 (2017).
20. B. Escudero-Perez *et al.*, Comparative pathogenesis of Ebola virus and Reston virus infection in humanized mice. *JCI Insight* **4**, (2019).
21. S. Baize *et al.*, Inflammatory responses in Ebola virus-infected patients. *Clin Exp Immunol* **128**, 163-168 (2002).
22. L. E. Hensley, H. A. Young, P. B. Jahrling, T. W. Geisbert, Proinflammatory response during Ebola virus infection of primate models: possible involvement of the tumor necrosis factor receptor superfamily. *Immunol Lett* **80**, 169-179 (2002).
23. A. K. McElroy *et al.*, Macrophage Activation Marker Soluble CD163 Associated with Fatal and Severe Ebola Virus Disease in Humans(1). *Emerg Infect Dis* **25**, 290-298 (2019).
24. D. Kotliar *et al.*, Single-Cell Profiling of Ebola Virus Disease In Vivo Reveals Viral and Host Dynamics. *Cell*, (2020).
25. J. C. Kash *et al.*, Global suppression of the host antiviral response by Ebola- and Marburgviruses: increased antagonism of the type I interferon response is associated with enhanced virulence. *J Virol* **80**, 3009-3020 (2006).
26. A. L. Hartman, L. Ling, S. T. Nichol, M. L. Hibberd, Whole-genome expression profiling reveals that inhibition of host innate immune response pathways by Ebola virus can be reversed by a single amino acid change in the VP35 protein. *J Virol* **82**, 5348-5358 (2008).

27. M. Holzer *et al.*, Differential transcriptional responses to Ebola and Marburg virus infection in bat and human cells. *Sci Rep* **6**, 34589 (2016).
28. I. V. Kuzmin *et al.*, Innate Immune Responses of Bat and Human Cells to Filoviruses: Commonalities and Distinctions. *J Virol* **91**, (2017).
29. S. Marozin *et al.*, Inhibition of the IFN-beta response in hepatocellular carcinoma by alternative spliced isoform of IFN regulatory factor-3. *Mol Ther* **16**, 1789-1797 (2008).
30. S. Marozin *et al.*, Cell cycle progression or translation control is not essential for vesicular stomatitis virus oncolysis of hepatocellular carcinoma. *PLoS One* **5**, e10988 (2010).
31. B. Israelow, C. M. Narbus, M. Sourisseau, M. J. Evans, HepG2 cells mount an effective antiviral interferon-lambda based innate immune response to hepatitis C virus infection. *Hepatology* **60**, 1170-1179 (2014).
32. K. Li, Z. Chen, N. Kato, M. Gale, Jr., S. M. Lemon, Distinct poly(I-C) and virus-activated signaling pathways leading to interferon-beta production in hepatocytes. *J Biol Chem* **280**, 16739-16747 (2005).
33. S. R. Khetani, S. N. Bhatia, Microscale culture of human liver cells for drug development. *Nat Biotechnol* **26**, 120-126 (2008).
34. S. March *et al.*, Micropatterned coculture of primary human hepatocytes and supportive cells for the study of hepatotropic pathogens. *Nat Protoc* **10**, 2027-2053 (2015).
35. N. Gural *et al.*, In Vitro Culture, Drug Sensitivity, and Transcriptome of Plasmodium Vivax Hypnozoites. *Cell Host Microbe* **23**, 395-406 e394 (2018).
36. E. Michailidis *et al.*, Expansion, in vivo-ex vivo cycling, and genetic manipulation of primary human hepatocytes. *Proc Natl Acad Sci U S A* **117**, 1678-1688 (2020).
37. R. E. Schwartz *et al.*, Modeling hepatitis C virus infection using human induced pluripotent stem cells. *Proc Natl Acad Sci U S A* **109**, 2544-2548 (2012).
38. A. Shlomai *et al.*, Modeling host interactions with hepatitis B virus using primary and induced pluripotent stem cell-derived hepatocellular systems. *Proc Natl Acad Sci U S A* **111**, 12193-12198 (2014).
39. A. A. Wilson *et al.*, Emergence of a stage-dependent human liver disease signature with directed differentiation of alpha-1 antitrypsin-deficient iPS cells. *Stem Cell Reports* **4**, 873-885 (2015).
40. F. Sakurai *et al.*, Human induced-pluripotent stem cell-derived hepatocyte-like cells as an in vitro model of human hepatitis B virus infection. *Sci Rep* **7**, 45698 (2017).
41. X. Zhou *et al.*, Modulating innate immunity improves hepatitis C virus infection and replication in stem cell-derived hepatocytes. *Stem Cell Reports* **3**, 204-214 (2014).
42. J. Lang, D. Vera, Y. Cheng, H. Tang, Modeling Dengue Virus-Hepatic Cell Interactions Using Human Pluripotent Stem Cell-Derived Hepatocyte-like Cells. *Stem Cell Reports* **7**, 341-354 (2016).
43. T. Tricot, N. Helsen, S. J. F. Kaptein, J. Neyts, C. M. Verfaillie, Human stem cell-derived hepatocyte-like cells support Zika virus replication and provide a relevant model to assess the efficacy of potential

antivirals. *PLoS One* **13**, e0209097 (2018).

44. P. O. Kwiterovich, Jr., The metabolic pathways of high-density lipoprotein, low-density lipoprotein, and triglycerides: a current review. *Am J Cardiol* **86**, 5L-10L (2000).
45. M. Ingelman-Sundberg, S. C. Sim, A. Gomez, C. Rodriguez-Antona, Influence of cytochrome P450 polymorphisms on drug therapies: pharmacogenetic, pharmacoepigenetic and clinical aspects. *Pharmacol Ther* **116**, 496-526 (2007).
46. M. T. Donato, R. Jover, M. J. Gomez-Lechon, Hepatic cell lines for drug hepatotoxicity testing: limitations and strategies to upgrade their metabolic competence by gene engineering. *Curr Drug Metab* **14**, 946-968 (2013).
47. A. X. Chen, Chhabra, A., Greco Song, H-H., Fleming, H. E., Chen, C.S., Bhatia, S.N., Controlled Apoptosis of Stromal Cells to Engineer Human Microlivers. *Advanced Functional Materials* **30**, 1-10 (2020).
48. F. Wang *et al.*, RNAscope: a novel in situ RNA analysis platform for formalin-fixed, paraffin-embedded tissues. *J Mol Diagn* **14**, 22-29 (2012).
49. A. J. Hume, E. Muhlberger, Distinct Genome Replication and Transcription Strategies within the Growing Filovirus Family. *J Mol Biol*, (2019).
50. E. V. Nelson *et al.*, Ebola Virus Does Not Induce Stress Granule Formation during Infection and Sequesters Stress Granule Proteins within Viral Inclusions. *J Virol* **90**, 7268-7284 (2016).
51. L. Kolesnikova, A. Nanbo, S. Becker, Y. Kawaoka, Inside the Cell: Assembly of Filoviruses. *Curr Top Microbiol Immunol* **411**, 353-380 (2017).
52. J. S. Towner *et al.*, Generation of eGFP expressing recombinant Zaire ebolavirus for analysis of early pathogenesis events and high-throughput antiviral drug screening. *Virology* **332**, 20-27 (2005).
53. J. Olejnik *et al.*, Ebolaviruses Associated with Differential Pathogenicity Induce Distinct Host Responses in Human Macrophages. *J Virol* **91**, (2017).
54. R. Channappanavar *et al.*, Dysregulated Type I Interferon and Inflammatory Monocyte-Macrophage Responses Cause Lethal Pneumonia in SARS-CoV-Infected Mice. *Cell Host Microbe* **19**, 181-193 (2016).
55. I. E. Galani *et al.*, Untuned antiviral immunity in COVID-19 revealed by temporal type I/III interferon patterns and flu comparison. *Nat Immunol* **22**, 32-40 (2021).
56. D. Power *et al.*, IFI44 suppresses HIV-1 LTR promoter activity and facilitates its latency. *Virology* **481**, 142-150 (2015).
57. C. Carlton-Smith, R. M. Elliott, Viperin, MTAP44, and protein kinase R contribute to the interferon-induced inhibition of Bunyamwera Orthobunyavirus replication. *J Virol* **86**, 11548-11557 (2012).
58. D. C. Busse *et al.*, Interferon-Induced Protein 44 and Interferon-Induced Protein 44-Like Restrict Replication of Respiratory Syncytial Virus. *J Virol* **94**, (2020).
59. Y. Liao, J. Wang, E. J. Jaehnig, Z. Shi, B. Zhang, WebGestalt 2019: gene set analysis toolkit with revamped UIs and APIs. *Nucleic Acids Res* **47**, W199-W205 (2019).

60. J. Olejnik *et al.*, Filovirus Strategies to Escape Antiviral Responses. *Curr Top Microbiol Immunol*, (2017).
61. U. Ben-David *et al.*, Genetic and transcriptional evolution alters cancer cell line drug response. *Nature* **560**, 325-330 (2018).
62. A. K. McElroy, E. Muhlberger, C. Munoz-Fontela, Immune barriers of Ebola virus infection. *Curr Opin Virol* **28**, 152-160 (2018).
63. I. S. Caballero *et al.*, In vivo Ebola virus infection leads to a strong innate response in circulating immune cells. *BMC Genomics* **17**, 707 (2016).
64. A. K. McElroy *et al.*, Kinetic Analysis of Biomarkers in a Cohort of US Patients With Ebola Virus Disease. *Clin Infect Dis* **63**, 460-467 (2016).
65. L. D. Jasenosky *et al.*, The FDA-Approved Oral Drug Nitazoxanide Amplifies Host Antiviral Responses and Inhibits Ebola Virus. *iScience* **19**, 1279-1290 (2019).
66. H. Feldmann, T. W. Geisbert, Ebola haemorrhagic fever. *Lancet* **377**, 849-862 (2011).
67. T. W. Geisbert *et al.*, Treatment of Ebola virus infection with a recombinant inhibitor of factor VIIa/tissue factor: a study in rhesus monkeys. *Lancet* **362**, 1953-1958 (2003).
68. N. A. Twenhafel *et al.*, Pathology of experimental aerosol Zaire ebolavirus infection in rhesus macaques. *Vet Pathol* **50**, 514-529 (2013).
69. M. D. Ward *et al.*, Characterization of the plasma proteome of nonhuman primates during Ebola virus disease or melioidosis: a host response comparison. *Clin Proteomics* **16**, 7 (2019).
70. T. W. Geisbert *et al.*, Pathogenesis of Ebola hemorrhagic fever in primate models: evidence that hemorrhage is not a direct effect of virus-induced cytolysis of endothelial cells. *Am J Pathol* **163**, 2371-2382 (2003).
71. A. Jankeel *et al.*, Early Transcriptional Changes within Liver, Adrenal Gland, and Lymphoid Tissues Significantly Contribute to Ebola Virus Pathogenesis in Cynomolgus Macaques. *J Virol* **94**, (2020).
72. S. F. Boj, M. Parrizas, M. A. Maestro, J. Ferrer, A transcription factor regulatory circuit in differentiated pancreatic cells. *Proc Natl Acad Sci U S A* **98**, 14481-14486 (2001).
73. K. J. Jang *et al.*, Reproducing human and cross-species drug toxicities using a Liver-Chip. *Sci Transl Med* **11**, (2019).

Figures

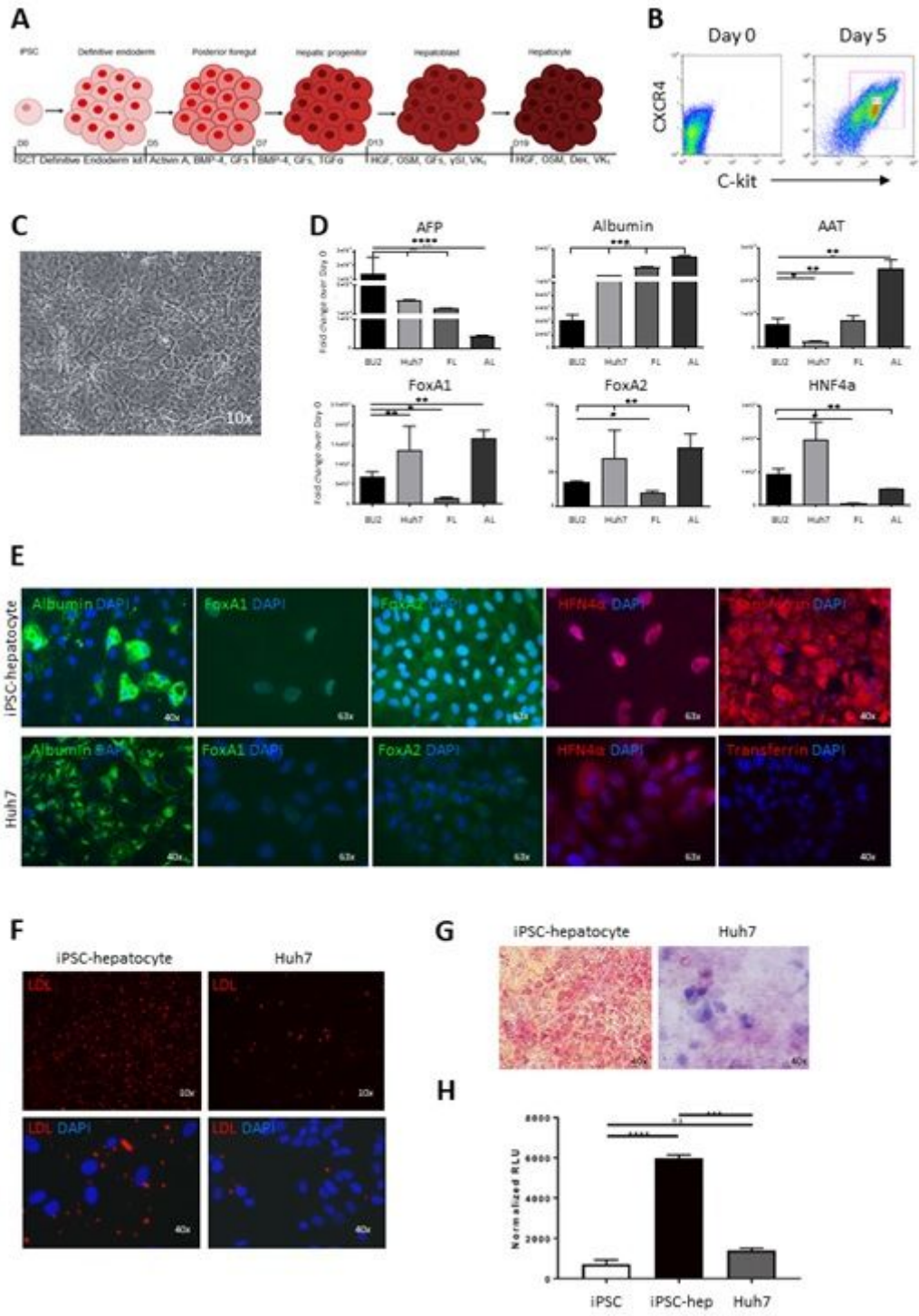

Figure 1

iPSC-derived hepatocytes display molecular hepatic identity and retain hepatic functions. (A) Outline of the directed differentiation protocol used to generate iPSC-derived hepatocytes. SCT, StemCell Technologies; GFs (Growth Factors): FGF-2, VEGF, EGF; Dex, dexamethasone; VK1, vitamin K; OSM, Oncostatin M. (B) Representative flow cytometry analysis of D0 and D5 iPSC differentiation into endoderm stained for definitive endoderm markers CXCR4 and c-kit. (C) Brightfield image of iPSC-derived hepatocytes at D23. Scale Bar is 200 μm. D) Taqman qRT-PCR analysis of iPSC-derived hepatocytes at D23, Huh7 cells, fetal liver, and adult liver. Expression of each marker is normalized to β-actin and

visualized as the fold change over D0 iPSCs. * p ≤ 0.05; ** p ≤ 0.01; *** p ≤ 0.001; **** p ≤ 0.0001. (E) Expression of albumin, FOXA1, FOXA2, HNF4α, and transferrin determined by immunofluorescence analysis in iPSC-derived hepatocytes (top row) and Huh7 cells (bottom row). Representative images of biological duplicates. Images taken at 40x magnification or 63x magnification with oil, scale bars are 100 μm. (F) Representative images of LDL-uptake assay for iPSC-derived hepatocytes and Huh7 cells. LDL analog fluoresces red when endocytosed into the cell. Images taken at 10x (top row, scale bar = 200 μm) and 40x magnification (bottom row, scale bar = 100 μm). Cell nuclei were stained with DAPI. (G) Representative PAS staining of iPSC-derived hepatocytes and Huh7 cells. Images taken at 40x magnification, scale bar is 100 μm. (H) Detection of active CY3A4 in iPSC-derived hepatocytes and Huh7 cells using a P450-Glo assay. Relative luciferase units (RLU) for each sample were normalized to RLU from supernatants of untreated cells. Error bars represent three technical replicates. ns, not significant; *** p ≤ 0.001; **** p ≤ 0.0001.

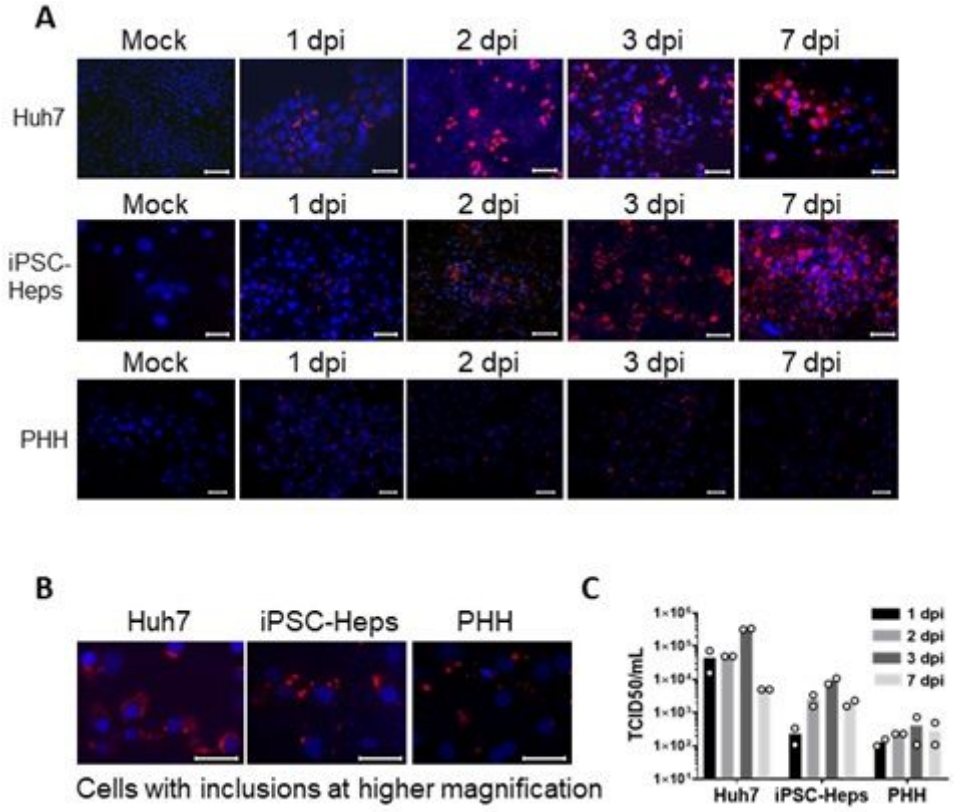

Figure 2

iPSC-derived hepatocytes and PHH are susceptible to EBOV infection. (A) Immunofluorescence analysis of EBOV-infected Huh7 cells, iPSC-derived hepatocytes, and PHH. Cells were mock-infected or infected with EBOV at an MOI of 10, fixed at the indicated time points, and stained with an antibody directed against EBOV nucleoprotein (red). Cell nuclei were stained with DAPI. Images are representative of triplicate experiments. Images of iPSC-derived hepatocytes and Huh7 cells taken at 40x magnification. Images of PHHs taken at 20x magnification. Scale bar is 20 μm. (B) Higher magnification to visualize viral inclusions. Images taken at 63x magnification. Scale bar is 20 μm. (C) Viral titers of each EBOV-

infected hepatocyte platform at the indicated time points. Bars represent the average of two technical replicates.

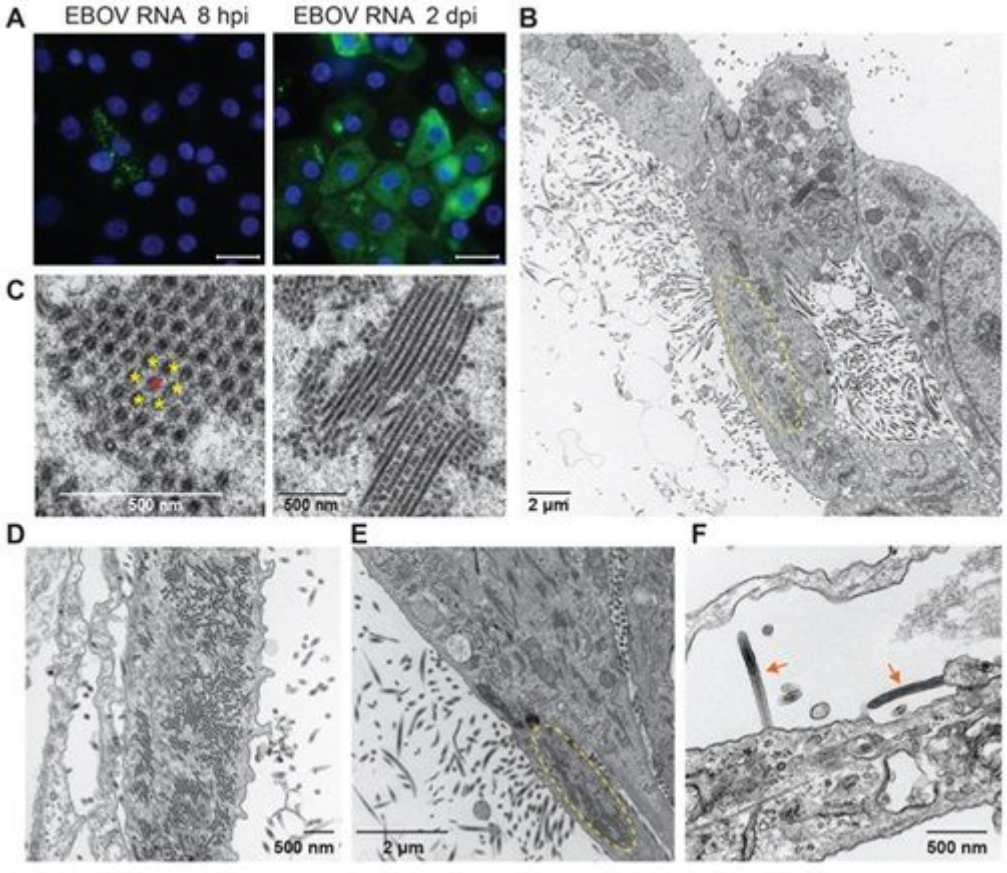

Figure 3

Productive EBOV infection of iPSC-derived hepatocytes. (A) RNA FISH analysis of EBOV-infected iPSC-derived hepatocytes at the indicated time points using probes directed against EBOV VP35 mRNA. Scale bar is 20 µm. (B-F) Transmission electron microscopy of EBOV-infected iPSC-derived hepatocytes at 1 and 2 dpi. Cells were infected with an MOI of 3. (B) Overview of EBOV-infected cell at 2 dpi. Circled area indicates the accumulation of filamentous viral nucleocapsids into inclusions. (C) Higher magnification of cross sectioned (left) and longitudinal sectioned (right) viral inclusions. Single nucleocapsids are marked with yellow and red asterisks, respectively, to visualize the hexagonal pattern. (D, E) Release of viral particles at 1 dpi (D) and 2 dpi (E). Circled area in (E) indicates viral inclusions. (F) Arrows indicate mature, budding Ebola virions. Cells were fixed 2 dpi. Images were taken from cells derived from different donors (A-D, donor BU2; E, donor BU1; F, donor BU3).

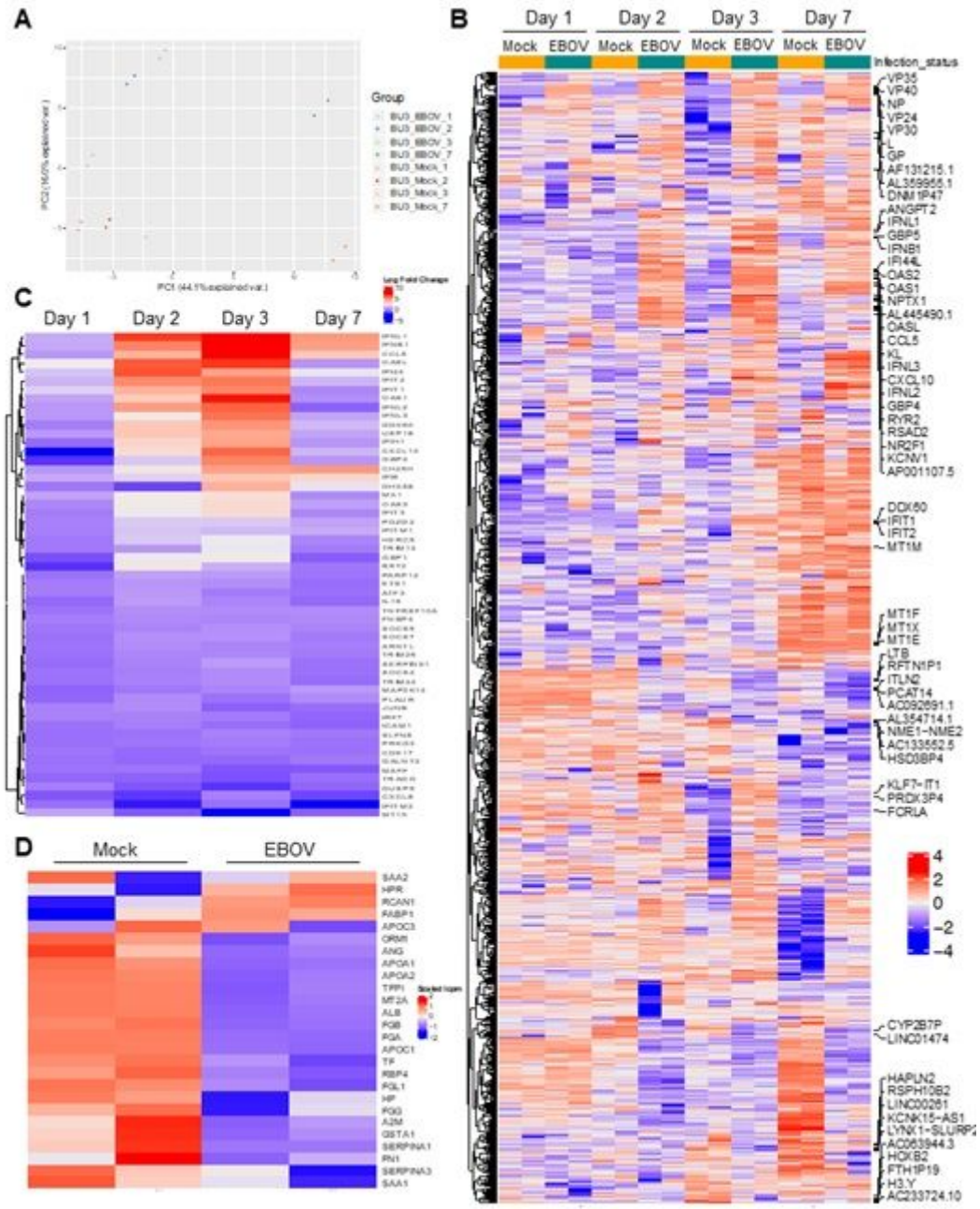

Figure 4

Upregulation of ISGs and downregulation of genes involved in liver function in EBOV-infected iPSC-derived hepatocytes at 2 and 3 dpi. (A) Principle component analysis (PCA) of transcriptional responses of EBOV- and mock-infected iPSC-derived hepatocytes at each time point. PCA1 represents the majority of variance and is associated with the day of differentiation. PCA2 represents the second largest contributor of variance and is associated with infection status. (B) Heatmap displaying the 250 most variable genes at each time point. Highlighted are the top 30 upregulated and downregulated DEG at 3 dpi. Key for the value of the logFC to the right of the plot. (C) Heatmap displaying the logFC for a list of ISGs (right of the plot) of EBOV-infected iPSC-derived hepatocytes compared to mock-infected cells at the indicated time points. Key logFC change in expression shown to the right. (D) Heatmap displaying the logFC for a list of genes involved in liver function (right of the plot) of mock- and EBOV-infected iPSC-

derived hepatocytes at 3 dpi. Shown are the technical replicates for each condition. Key logFC change in expression shown to the right.

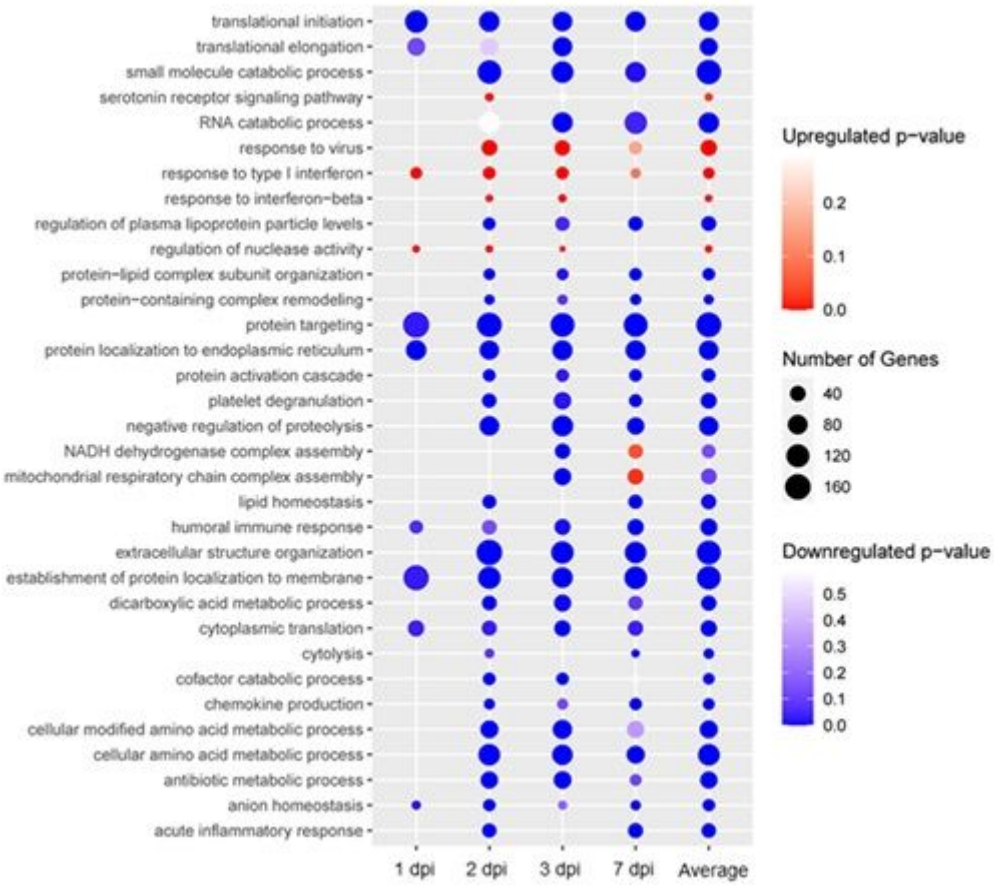

Figure 5

EBOV infection of iPSC-derived hepatocytes leads to a general downregulation of critical pathways with the exception of viral response pathways. Gene Ontology (GO) analysis of the DEGs in EBOV- compared to mock-infected iPSC-derived hepatocytes for each time point. FDR ≤ 0.01. Time point labeled on the bottom of the plot, GO pathways labeled on the left of the plot, key located on the right of the plot. Average represents the fold change of transcripts averaged across all EBOV-infected samples compared to the average expression of transcripts across all Mock infected samples.

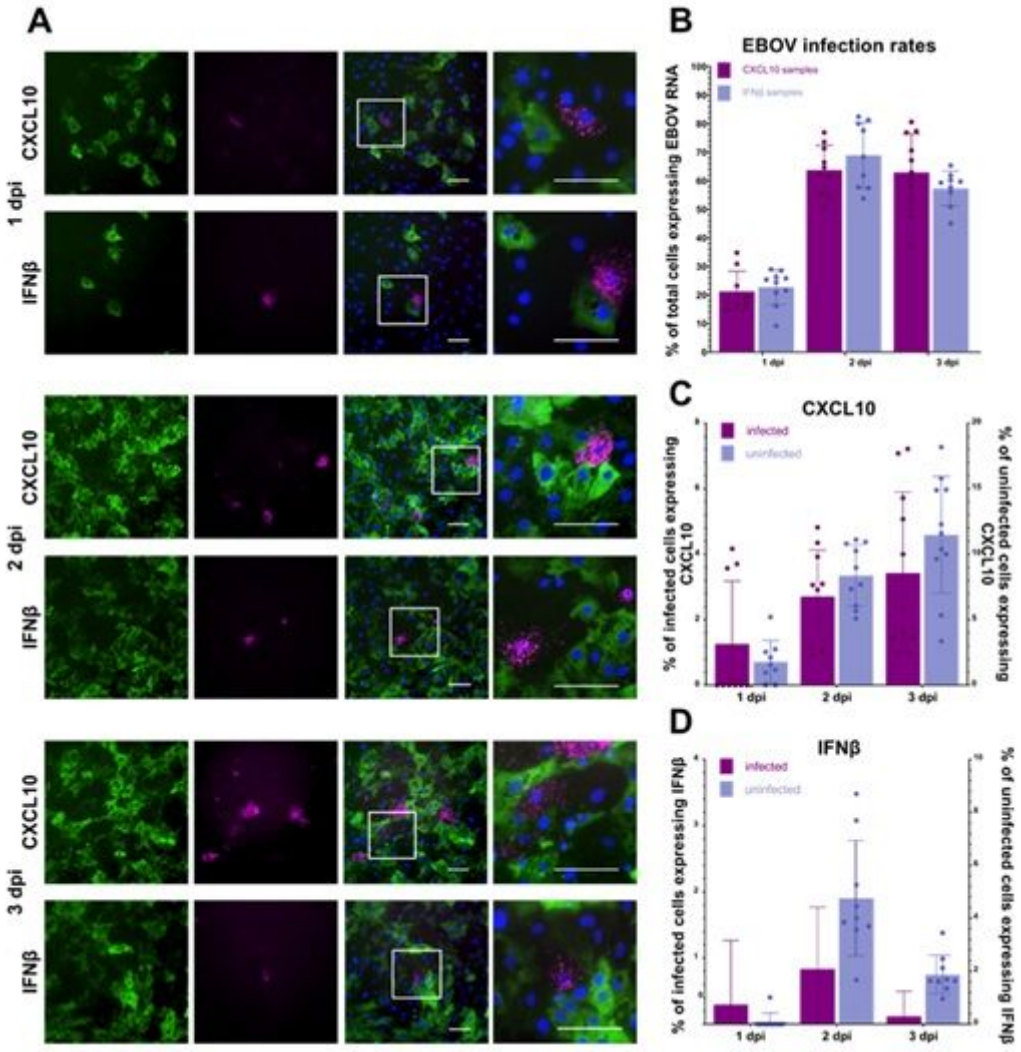

Figure 6

RNA FISH analysis reveals expression of IFNβ and CXCL10 in uninfected bystander cells and cells with weak EBOV mRNA signal intensity. (A) EBOV-infected iPSC-derived hepatocytes were fixed at the indicated times and analyzed by RNA FISH using a combination of probes against EBOV VP35 mRNA (green) and CXCL10 (magenta, top row) or IFNβ (magenta, bottom row) mRNA. Shown are representative images at 20x magnification, and right column shows inset region of merged images. Size bars = 100 µm. (B-D) Quantification of gene expression from images using at least 1,200 cells and eight fields of view per time point and probe combination. (B) Percentage of total cells positive for EBOV VP35 mRNA at each time point. (C) Percentage of infected cells expressing CXCL10 mRNA, left axis, and percentage of uninfected cells expressing CXCL10 mRNA, right axis. (D) Percentage of infected cells expressing IFNβ mRNA, left axis, and percentage of uninfected cells expressing IFNβ mRNA, right axis.

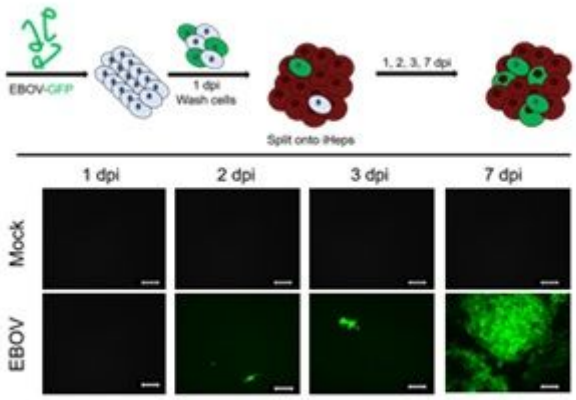

Figure 7

Transmission of EBOV-GFP from monocyte-derived macrophages (MDM) to iPSC-derived hepatocytes. Top, infection scheme and workflow. Live fluorescent imaging of MDM and iPSC-derived hepatocyte co-cultures at various time points p.i. 10x magnification. Images taken from one well over the period of 1-7 dpi. Scale bar is 20 µm. Images are representative of 2 independent experiments.

Supplementary Files

This is a list of supplementary files associated with this preprint. Click to download.

- SupplementaryInformation.pdf